

Nonperturbative potential for the study of quarkonia in QGP

Dibyendu Bala^{*} and Saumen Datta[†]

*Department of Theoretical Physics, Tata Institute of Fundamental Research,
Homi Bhabha Road, Mumbai 400005, India*

 (Received 11 October 2019; accepted 21 January 2020; published 10 February 2020)

A thermal potential can be defined to facilitate understanding the behavior of quarkonia in quark-gluon plasma. A nonperturbative evaluation of this potential from lattice QCD is difficult, as it involves a real-time correlation function, and has often involved the use of Bayesian analysis, with its associated systematics. In this work we show that using the properties of the static quarkonia thermal correlation functions, one can directly extract a thermal potential for quarkonia from Euclidean Wilson loop data. This leads to a controlled extraction and allows us to judge the suitability of various model potentials.

DOI: [10.1103/PhysRevD.101.034507](https://doi.org/10.1103/PhysRevD.101.034507)

I. INTRODUCTION

Quarkonia, mesonic bound states of heavy quark and antiquark, have played a very important role in our understanding of the physics of strong interactions. The experimental signatures of some of these states are distinctive, the most iconic being the dilepton peak of the vector quarkonia. In the theoretical side, the heavy quark mass, $M_Q \gg \Lambda_{\text{QCD}}$, leads to simplifications. The earliest insights about properties of quarkonia were obtained by treating them as nonrelativistic states bound by a color electric potential. The potential suitable for studies of quarkonia has been calculated in detail using numerical Monte Carlo studies on lattice-regularized QCD; see, e.g., Ref. [1] for a review. The potential remains an important ingredient in a systematic expansion of quarkonia in $1/M_Q$ [2].

The dilepton peaks of the vector quarkonia, in particular that of the J/ψ , have been extremely important signatures of creation of quark-gluon plasma (QGP) in ultrarelativistic heavy ion collisions (URHIC), following the suggestion three decades ago [3] that the screening of the color charge inside QGP will lead to the dissolution of bound states. This was made more quantitative in follow-up studies [4]. The early studies used a perturbative Debye-screened form,

$$V_T^{\text{re}}(\vec{r}) = -\frac{\alpha(T)}{r} e^{-m_D r}, \quad (1)$$

^{*}dibyendu.bala@tifr.res.in

[†]saumen@theory.tifr.res.in

Published by the American Physical Society under the terms of the Creative Commons Attribution 4.0 International license. Further distribution of this work must maintain attribution to the author(s) and the published article's title, journal citation, and DOI. Funded by SCOAP³.

which is the free energy of a static $Q\bar{Q}$ pair in perturbative QGP. Here m_D is the Debye mass, $\alpha = \frac{4}{3} \frac{g^2}{4\pi}$, and g is evaluated at a scale determined by the temperature T . Nonperturbatively, the free energy of the $Q - \bar{Q}$ pair in plasma was calculated using lattice QCD [5], which was used as a proxy for an effective finite temperature potential. However, in the early days a proper formalism for the potential-based study of quarkonia in QGP was missing. In particular, other thermodynamic quantities can be derived from the free energy, e.g., an “internal energy” for the $Q\bar{Q}$ pair [6]; the use of such quantities have also been explored in the literature [7].

A theoretical formalism for an “effective finite temperature potential,” which is connected to experimentally observed quantities such as the dilepton rate, was first provided in Ref. [8]. The starting point is a point-split version of the dilepton current,

$$J_{\vec{r}}^{\mu}(t, \vec{x}) = \bar{Q} \left(t, \vec{x} + \frac{\vec{r}}{2} \right) \gamma^{\mu} \mathbb{U} \left(t; \vec{x} + \frac{\vec{r}}{2}, \vec{x} - \frac{\vec{r}}{2} \right) Q \left(t, \vec{x} - \frac{\vec{r}}{2} \right), \quad (2)$$

where \mathbb{U} is a suitable gauge connection such that V^{μ} is gauge invariant and the angular brackets denote a thermal average. Defining the correlation function

$$C_{>}(t, \vec{r}) = \int d^3x \langle J_{\vec{r}}^{\mu}(t, \vec{x}) J_{\mu, \vec{r}}(0, \vec{x}) \rangle, \quad (3)$$

the spectral function $\rho_J(\omega, \vec{r}; T)$ is defined from its Fourier transform,

$$\rho_J(\omega, \vec{r}; T) = (1 - e^{-\omega/T}) \int dt e^{i\omega t} C_{>}(t, \vec{r}). \quad (4)$$

The dilepton rate is proportional to the spectral function of the point current, $\rho(\omega; T) = \lim_{\vec{r} \rightarrow 0} \rho_J(\omega, \vec{r}; T)$.

Since we are interested in heavy quarks with $M_Q \gg T$, Λ_{QCD} , Eq. (3) simplifies. Going to the nonrelativistic notation $Q = (\psi/\chi)$ where ψ, χ are nonrelativistic fields that annihilate a quark and create an antiquark, respectively, and remembering that since $M_Q \gg T$, the thermal states do not include Q fields, the leading (M_Q^0) term in an $1/M_Q$ expansion gives

$$C_>(t, \vec{r}) \equiv \int d^3x \left\langle \chi^\dagger \left(t, \vec{x} - \frac{\vec{r}}{2} \right) \sigma_k \mathbb{U}^\dagger \psi \left(t, \vec{x} + \frac{\vec{r}}{2} \right) \times \psi^\dagger \left(0, \vec{x} + \frac{\vec{r}}{2} \right) \sigma_k \mathbb{U} \chi \left(0, \vec{x} - \frac{\vec{r}}{2} \right) \right\rangle. \quad (5)$$

If one has a system where the sole interaction term is a potential $V(\vec{r})$ between the quark and the antiquark, then it is easy to show that, to leading order in $1/M_Q$, $C_>(t, \vec{r})$ satisfies [9]

$$\left(i\partial_t - \frac{\nabla_{\vec{r}}^2}{M_Q} \right) C_>(t, \vec{r}) = V(\vec{r}) C_>(t, \vec{r}). \quad (6)$$

In our theory where the $Q\bar{Q}$ are interacting with the thermal medium, we can then define a potential by equating the left-hand side of Eq. (6) to $V(t, \vec{r}) C_>(t, \vec{r})$ (staying within leading order of $1/M_Q$), where the interaction effects are summarized in a time-dependent $V(t, \vec{r})$. An effective thermal potential, $V_T(\vec{r})$, can then be defined in the large t limit, if the limit exists: $V_T(\vec{r}) = \lim_{t \rightarrow \infty} V(t, \vec{r})$.

The potential $V_T(\vec{r})$ can be obtained by going to the static limit, where modulo renormalization factor, $C_>(t, \vec{r})$, reduces to a Minkowski-time Wilson loop,

$$W_M(t, \vec{r}) = \frac{1}{3} \text{Tr} \mathbb{P} e^{i \int_0^t dt_1 A_0(t_1, \vec{r}/2)} \mathbb{U}(t; \vec{r}/2, -\vec{r}/2) \times \mathbb{P} e^{i \int_t^0 dt_2 A_0(t_2, -\vec{r}/2)} \mathbb{U}(0; -\vec{r}/2, \vec{r}/2), \quad (7)$$

and Eq. (6) reduces to

$$i\partial_t \log W_M(t, \vec{r}) \xrightarrow{t \rightarrow \infty} V_T(\vec{r}), \quad (8)$$

which defines our thermal potential [8,9]. Using $V_T(\vec{r})$ to calculate $C_>(t, \vec{r})$ from Eq. (6) will give the resummation of the leading ladder diagrams.

A calculation of $V_T(\vec{r})$ in leading order hard thermal loop (HTL) perturbation theory gives [8]

$$V_T(\vec{r}) = V_T^{\text{re}}(\vec{r}) - iV_T^{\text{im}}(\vec{r}), \quad \text{where} \\ V_T^{\text{im}}(\vec{r}) = \alpha T \times \int_0^\infty dz \frac{2z}{(z^2 + 1)^2} \left[1 - \frac{\sin(zm_D r)}{zm_D r} \right] \quad (9)$$

and $V_T^{\text{re}}(\vec{r})$ is given in Eq. (1). In Eq. (9) we have absorbed a negative sign in the definition of $V_T^{\text{im}}(\vec{r})$, so that $V_T^{\text{im}}(\vec{r})$ takes positive values. $V_T^{\text{re}}(\vec{r})$ corresponds to the usual physics of Debye screening in medium, such that for sufficiently large screening, the bound states will not form. On the other hand, $V_T^{\text{im}}(\vec{r})$ clearly leads to a broadening of the spectral function peak [10]. It captures the physics of collision with the thermal particles leading to a decoherence of the $Q\bar{Q}$ wave function [11–13]. For the quark and antiquark far apart, $r \gg T$, $V_T^{\text{im}}(\vec{r})$ reaches a finite limit αT giving the damping rate of the individual quarks [9].

It is well-known that the perturbative calculation, Eq. (9), is not suitable at temperatures \lesssim a few times T_c , the deconfinement temperature. The aim of this paper is to make a nonperturbative calculation of an effective thermal potential, using numerical lattice gauge theory techniques. Following the insight of Ref. [8], various authors have tried calculating the thermal potential nonperturbatively. In the next section we will outline our strategy. More details, and some discussion on difference from earlier studies, can be found in Sec. IV.

The potential description, Eq. (6), provides only the leading order approximation to Eq. (3) in an expansion in $1/M_Q$ and (in the perturbative language) accounts for a subclass of diagrams. At zero temperature, the justification for this is well understood. At finite temperature, extra scales come into play, making the picture more complicated. A systematic, effective field theory based study of the interplay of these scales has been made in Ref. [14] in perturbation theory. In the hierarchy of scales

$$M \gg \pi T \gg 1/r_B \gtrsim m_D \sim gT \gg E_B$$

one gets the potential Eq. (9), where r_B is the radius of the bound state and E_B the binding energy. For the temperatures of interest in heavy ion collision experiments, this hierarchy of scales is hardly satisfied. The effective field theory version, however, is perturbative and therefore cannot be directly used for phenomenology.

Instead of going through such an approximation, one could instead try to directly calculate the spectral function from the Euclidean $\langle J_\mu J_\mu \rangle$ correlation function. This has been attempted for charmonia [15,16] and, using nonrelativistic QCD (NRQCD), for bottomonia [17,18]. Unfortunately, the extraction of a spectral function from the Euclidean correlator is a notoriously difficult problem, and the systematics are large (see [19] for a discussion, and [20] for early comparison of potential model results with results of [15]). A nonperturbatively determined potential allows one to study the in-medium modification of the spectral function for sufficiently heavy quarks and has been used for quarkonia phenomenology; see, e.g., [21].

Note that the spectral function obtained through Eqs. (4) and (6) treats the $Q\bar{Q}$ pair as an external probe in an equilibrium plasma. A proper dynamical treatment should

take into account the simultaneous evolution of the system and the $\bar{Q}Q$ pair. This can be formulated in the language of an open quantum system [11,13,22–24]. The potential remains an important structure in such frameworks [22,24]. In particular, a microscopic understanding of Eq. (6) can be obtained in such a framework by introducing the collision of the plasma constituents with the $Q\bar{Q}$ through a statistical noise term [11,12]. $V_T^{\text{im}}(\vec{r})$ then controls the correlation of the noise term, and Eq. (4) is understood to be the noise-averaged version of the $Q\bar{Q}$ -plasma interaction.

The plan of the rest of the paper is as follows. After explaining the calculational methodology in the next section, in Sec. III we will give the calculational details. Section IV will give our results for the potential. Some phenomenological discussions and implications of the potential obtained will be discussed in Sec. V, and the last section will have a summary and discussion.

II. NONPERTURBATIVE STUDY OF FINITE TEMPERATURE POTENTIAL

The potential $V_T(\vec{r})$ is directly related to the Minkowski space Wilson loop, Eq. (8). But in numerical Monte Carlo studies we work in Euclidean space. At zero temperature, it is straightforward to calculate the $Q\bar{Q}$ potential from the Euclidean Wilson loop:

$$W(\tau, \vec{r}) \xrightarrow{\tau \rightarrow \infty} C(\vec{r}) e^{-\tau V(\vec{r})}. \quad (10)$$

At finite temperature, the simple spectral decomposition outlined in Eq. (10) does not work. The first attempt to extract the $Q\bar{Q}$ potential from $W_T(\tau, \vec{r})$ was carried out in Ref. [25]. The spectral decomposition of the Minkowski-time loop leads to [25]

$$\begin{aligned} W_T(\tau, \vec{r}) &= \int_{-\infty}^{\infty} d\omega e^{-\omega\tau} \rho(\omega, \vec{r}; T) \\ \Rightarrow V_T(\vec{r}) &= -\partial_\tau \log W_T(\tau, \vec{r}) \\ &= \frac{\int_{-\infty}^{\infty} d\omega \omega e^{-\omega\tau} \rho(\omega, \vec{r}; T)}{\int_{-\infty}^{\infty} d\omega e^{-\omega\tau} \rho(\omega, \vec{r}; T)}. \end{aligned} \quad (11)$$

Bayesian techniques were used to extract $\rho(\omega, \vec{r}; T)$ from $W_T(\tau, \vec{r})$, and then calculate the potential using Eq. (11).

The reconstruction of $\rho(\omega, \vec{r}; T)$ from $W_T(\tau, \vec{r})$ is a notoriously unstable problem. To make matters worse, the quality of the Wilson loop data deteriorates quickly at large τ (this problem can be somewhat alleviated with recent numerical techniques [26]). While very impressive technological improvements have occurred in the Bayesian analysis techniques, the results obtained for potential still have stability issues or have large error bars, especially for $V_T^{\text{im}}(\vec{r})$. The first calculations [25] employed a Bayesian analysis method similar to maximum entropy and fitted the spectral function peak with a Lorentzian form. The results

obtained, however, are substantially different from a later analysis [27] that is of similar philosophy but employs a slightly different Bayesian analysis and fits to a skew-Lorentzian form [28]. The state-of-the-art for calculations in the gluonic plasma follows a similar methodology and can be seen in Ref. [29]. Studies have also been carried out for full QGP (i.e., with thermal quarks), both with a Lorentzian form of the spectral function [30] and using Bayesian reconstruction methods [31]. While the improvement in the analysis method has been impressive, the results still suffer from stability issues; in particular, it is not easy to disentangle the effects of $V_T^{\text{im}}(\vec{r})$ and $V_T^{\text{re}}(\vec{r})$ in $W_T(\tau, \vec{r})$.

In this paper we take a different approach. Let us motivate it by writing

$$W_T(\tau, \vec{r}) = e^{w(\tau, \vec{r})} W_T(\beta/2). \quad (12)$$

The physics of $V_T^{\text{re}}(\vec{r})$ is very similar to that of the zero temperature potential, Eq. (10). We therefore expect the real part of the potential to come from the part of $w(\tau, \vec{r})$ which has a linear behavior around $\beta/2$: $\tilde{w}(\tau, \vec{r}) \sim -(\tau - \beta/2) V_T^{\text{re}}(\vec{r}) + \dots$. We isolate the \tilde{w} part by splitting $W_T(\tau, \vec{r})$ as follows:

$$\begin{aligned} W_T(\tau, \vec{r}) &= W_T^a(\tau, \vec{r}) \times W_T^p(\tau, \vec{r}), \\ W_T^a(\tau, \vec{r}) &= \sqrt{\frac{W_T(\tau, \vec{r})}{W_T(\beta - \tau, \vec{r})}}, \\ W_T^p(\tau, \vec{r}) &= \sqrt{W_T(\tau, \vec{r}) \times W_T(\beta - \tau, \vec{r})}. \end{aligned} \quad (13)$$

We find that $B(\tau, \vec{r}) = \log W_T^a(\tau, \vec{r})$ has exactly the behavior we were expecting: $B(\tau, \vec{r}) \sim (\frac{\beta}{2} - \tau) V_T^{\text{re}}(\vec{r})$ over a large range of τ around $\beta/2$. We illustrate this in Fig. 1, where $B(\tau, \vec{r})/(\beta/2 - \tau)$ is plotted. We also checked that for configurations below T_c , where we can extract the potential from the full Wilson loop, $W_T^a(\tau, \vec{r})$ gives the same result but reaches the plateau sooner.

To understand the behavior of $W_T^p(\tau, \vec{r})$, we write a decomposition for $A(\tau, \vec{r}) = \log W_T^p(\tau, \vec{r})$:

$$\begin{aligned} A(\tau, \vec{r}) &= \int_{-\infty}^{\infty} d\omega \sigma(\omega; T) \frac{1}{2} (e^{-\omega\tau} + e^{-\omega(\beta-\tau)}) \\ &\quad + \tau\text{-independent terms}. \end{aligned} \quad (14)$$

To go to the potential, we follow the usual route of going to real time $\tau \rightarrow it$:

$$i\partial_t A(it) = \int_{-\infty}^{\infty} d\omega \sigma(\omega; T) \frac{\omega}{2} (e^{-i\omega t} - e^{-\omega\beta} e^{i\omega t}). \quad (15)$$

The potential is obtained in the large time limit of Eq. (15), when the oscillating factors $\exp(\pm i\omega t)$ ensure that only the $\omega \rightarrow 0$ contribution to the integral survives. In this limit

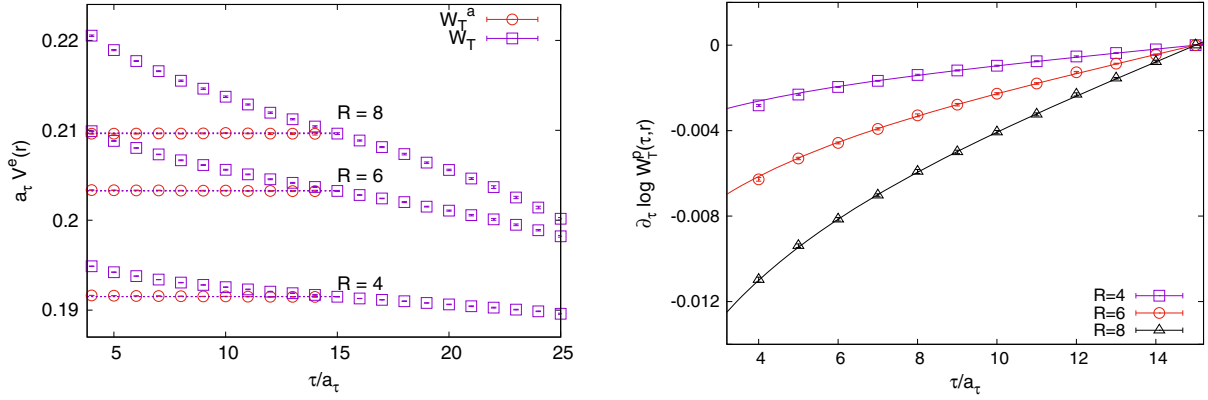


FIG. 1. (Left) “Local mass” plot from $W_T(\tau, \vec{r})$ and $W_T^a(\tau, \vec{r})$ for Set 3, $1.5 T_c$, at three different values of $R = r/a_s$. The results are from smeared Wilson loops. The dashed lines show the fitted mass. (Right) $\partial_\tau W_T^p(\tau, \vec{r})$ for the same set; the lines show the singular structure contribution [Eq. (17); see text].

$\exp(\beta\omega) \rightarrow 1$, and it is obvious from Eq. (15) that $A(it)$ leads to an imaginary potential. One can then extract the real and imaginary parts of the potential from $W_T^a(\tau, \vec{r})$ and $W_T^p(\tau, \vec{r})$, respectively [8],

$$\begin{aligned} V_T^{\text{re}}(\vec{r}) &= \lim_{t \rightarrow \infty} i \partial_t \log W_T^a(\tau, \vec{r})|_{\tau \rightarrow it}, \\ -iV_T^{\text{im}}(\vec{r}) &= \lim_{t \rightarrow \infty} i \partial_t \log W_T^p(\tau, \vec{r})|_{\tau \rightarrow it}. \end{aligned} \quad (16)$$

The argument above is motivated by perturbative studies of the potential, where the split Eq. (16) has been noted [8]. Even with Eq. (16), it is not obvious that the extraction of the potential from the Euclidean correlation function is simple; Eq. (16) involves large Minkowski time, while the non-perturbative data that can be obtained from the lattice are in Euclidean time $\tau \in [0, \beta)$. Successful extraction of the potential from Eq. (16) is contingent upon the contribution from the “potential modes” dominating the behavior of the correlation functions $A(\tau, \vec{r}), B(\tau, \vec{r})$. Fortunately, this is what was found in the behavior of the nonperturbative data. As we already discussed above and showed in Fig. 1, over a large range of τ , $W_T^a(\tau, \vec{r}) \sim \exp(-c\tau)$, leading to a straightforward extraction of $V_T^{\text{re}}(\vec{r})$ from the slope of the exponent. We actually obtained a very similar plateau in all our lattices. See Sec. IV A for more discussion.

One, of course, does not expect such a simple behavior from $A(\tau, \vec{r})$: Eq. (14) rules out a simple linear behavior near $\beta/2$. This is expected: if $W_T^p(\tau, \vec{r})$ had a linear exponential falloff, it would have contributed to a real potential. The large time behavior of $W_T^p(\tau \rightarrow it, \vec{r})$ can be inferred from a closer examination of Eq. (15), using the fact that in the limit of large t , $\exp(-i\omega t) - \exp(i\omega t - \omega\beta) \rightarrow -2\pi i\omega\delta(\omega)$. Then in order to get a potential $-iV_T^{\text{im}}(\vec{r}) = \lim_{t \rightarrow \infty} i \partial_t A(it)$ we need

$$\sigma(\omega; T) \underset{\omega \rightarrow 0}{\sim} \frac{1}{\omega^2} (1 + \mathcal{O}(\omega)). \quad (17)$$

Interestingly, this leading singularity structure gives a very good qualitative description of the τ dependence of $\partial_\tau A(\tau, \vec{r})$. This is illustrated in the right panel of Fig. 1.

The argument in this section is based on the assumption that a thermal potential can be defined using Eq. (8). We then make plausibility arguments on the structure of $W_T(\tau, \vec{r})$, and we show that the nonperturbative lattice data support this structure. The arguments leading to Eq. (16) can be made more concrete using Feynman diagrammatic language [9]: in Appendix B we outline this argument. There we also show the results of the leading order HTL perturbation calculation of $W_T(\tau, \vec{r})$ [8], which fully supports the structures of $A(\tau, \vec{r})$ and $B(\tau, \vec{r})$ discussed above, and which motivated this nonperturbative study. The $1/\omega^2$ behavior in Eq. (17) comes from the term $\frac{\rho(\omega)}{\omega^2}$ and a distribution function, $(1 + n_B(\omega)) \xrightarrow{\omega \rightarrow 0} \frac{T}{\omega}$, which follows from the structure of the time-ordered propagator [see Appendix B and Eq. (B4)]. It is connected to the scattering origin of the imaginary part of the potential, discussed below Eq. (9).

Our strategy for extraction of the potential is therefore straightforward: we extract $V_T^{\text{re}}(\vec{r})$ from a linear fit to $B(\tau, \vec{r})$, and to get $V_T^{\text{im}}(\vec{r})$, we expand $\sigma(\omega; T)$ in Eq. (14) in the basis $(1 + n_B(\omega))\{1/\omega, \omega, \dots\}$, and extract $V_T^{\text{im}}(\vec{r})$ from the coefficient of the most singular term. As Fig. 1 suggests, the leading terms dominate the data around $\beta/2$, allowing us to extract the potential relatively simply. We discuss further details in Sec. IV.

III. TECHNICAL DETAILS OF OUR STUDY

In this work, we have calculated the $Q\bar{Q}$ potential in a gluonic plasma, for moderately high temperatures $\leq 2T_c$. We have generated lattices with a spacetime anisotropic discretization with $\xi = a_s/a_\tau \approx 3$. A convenient algorithm for doing this is given in [32]. We follow this reference to estimate the lattice parameters we require. The anisotropy

is estimated nonperturbatively from the comparison of spatial and temporal Wilson loops [32], while a_τ is estimated from the string tension calculated from temporal Wilson loops. We use three sets of lattices, with a_τ ranging between $1/19T_c$ and $1/45T_c$. For each set, we change the temperature by changing N_τ , while keeping the spatial volume fixed.

For each set, we first make short Monte Carlo runs at closely spaced N_τ to find the N_τ for deconfinement transition. The final lattice sets used for the studies above T_c are shown in Table I. For much of this paper, we will measure all scales in units of T_c . However, for Sec. V we will need to quote physical units. We will do so by taking the string tension $\sigma = (0.44 \text{ GeV})^2$. This translates to a transition temperature $\sim 280 \text{ MeV}$. The spatial extent of the lattices are 1.44 fm or above. Some more details regarding the runs are given in Appendix A.

To determine the potential, we calculate thermal expectation values of timelike Wilson loops, i.e., the Euclidean time version of W_M in Eq. (8). It is well known that for the spatial connections \mathbb{U} straight thin-link gauge connections are not suitable: they lead to very noisy signals in numerical Monte Carlo studies. To alleviate the problem due to extended spatial connections, we do APE smearing [33]. This constitutes a replacement of the elementary gauge links U_i ,

$$U_i(\vec{x}, \tau) \rightarrow \text{Proj}_{SU(3)} \left\{ \alpha U_i(\vec{x}, \tau) + \sum_{\substack{1 \leq j \leq 3 \\ j \neq i}} (U_j(\vec{x}, \tau) U_i(\vec{x} + a_s \hat{j}, \tau) U_j^\dagger(\vec{x} + a_s \hat{i}, \tau) + U_j^\dagger(\vec{x} - a_s \hat{j}, \tau) U_i(\vec{x} - a_s \hat{j}, \tau) U_j(\vec{x} - a_s \hat{j} + a_s \hat{i}, \tau)) \right\} \quad (18)$$

iteratively. The spatial connections \mathbb{U} are then constructed from these smeared links. For this work, we have taken $\alpha = 2.5$.

TABLE I. Parameter sets for the finite temperature runs.

Set	β_s, β_t	N_s	N_t	T/T_c	L [fm]	a_t [fm]
I	2.469, 14.8	16	48	0.4	1.82	0.038
			24	0.8		
			16	1.2		
II	2.53, 15.95	24	48	0.6	1.73	0.024
			24	1.2		
			20	1.5		
III	2.6, 16.98	30	72	0.63	1.44	0.016
			60	0.75		
			38	1.2		
			30	1.5		
			23	2		

Note that Eq. ([18]) does not involve the time direction, and the time direction links are not smeared. So time slices and the definition of transfer matrix is not affected by the smearing. We use the multilevel algorithm [26] in the temporal direction: this allows us to get a good signal even for Wilson loops with a large time extent. For calculation of the potential at $T = 0$, smearing is routinely used, and the potential should be independent of the smearing. In the finite temperature case, the physical quantity one is interested in, the quarkonia peak in the dilepton channel, is independent of the details of the connection \mathbb{U} , as it is connected to the point current. We however, do a detailed study of the dependence of the potential on the smearing level in the next section.

In the literature, the correlator of Coulomb gauge fixed Wilson lines have often been used to extract the potential. The Coulomb gauge fixing can be formally understood as a dressing of the quark fields [34]:

$$\bar{\psi}(x)\psi(y)|_{\text{coul.}} \equiv \bar{\psi}_\Omega(x)\psi_\Omega(y), \quad (19)$$

where $\psi_\Omega(x) = \Omega(x)\psi(x)$ and $\Omega(x)$ is a dressing function such that $\psi_\Omega(x)$ is gauge invariant [34].

The Coulomb gauge potential has obvious advantages in that the extended spatial links are not there. At $T = 0$, it is also easy to argue (and has been well tested) that the Coulomb gauge potential agrees with the potential extracted from the Wilson loop. For $T > T_c$ such detailed comparison does not exist in the literature. Here we have made such a comparative study. The Coulomb gauge is fixed to an accuracy of 10^{-7} . We have also checked that the results do not change if the accuracy is made 10^{-6} or 10^{-9} instead. The potential from this Wilson line correlator has also been presented in Sec. IV. In particular, for the imaginary part of the potential, we observe differences between this potential and that obtained from the smeared Wilson loop. Since the Wilson loop operator does not involve dressing of the quark field, the connection to the point-point correlator at $\vec{r} \rightarrow 0$ is transparent. We use the potential obtained from the Wilson loop for further studies in Sec. V.

IV. POTENTIAL CALCULATED FROM WILSON LOOPS

In this section we present the details of our extraction of the potential, using Eq. (16). In Sec. IVA we discuss the real part of the potential. The results for the free energy of a $Q\bar{Q}$ pair is given in Sec. IV B, and the extraction of $V_T^{\text{im}}(\vec{r})$ is discussed in Sec. IV C. Besides quoting the results for the potential, we also compare the potential at different levels of smearing, and the results for Coulomb gauge. Finally, in Sec. IV D we will discuss the spectral representation Eq. (11) and touch on issues of direct extraction of spectral function from Euclidean data.

A. Real part of the potential

As outlined in Sec. II and Fig. 1, for smeared Wilson loops the extraction of the real part of the potential from $W_T^a(\tau, \vec{r})$ is straightforward. In the left panel of Fig. 2 we show the “local measurements” of $V_T^{\text{re}}(\vec{r})$ from Wilson loops at different levels of smearing. The error bars shown are from a jackknife analysis, after blocking the data to reduce autocorrelation. As the figure shows, while for a small number of APE smearing steps, the local mass takes time to reach a plateau, on increasing the number of steps a plateau is reached quickly, and we can easily extract the potential using a single exponent fit. While we have shown the local mass for one particular case, the effects are very similar for all our sets. For each smearing level the value obtained from the fit is shown by the horizontal band of the same color. The goodness of the fit, as demonstrated by χ^2 , is very good. The figure also shows that varying the number of smearing steps over a large range does not seem to have any statistically significant effect on the value reached at the plateau.

We also show in the figure the local values of the potential obtained from the Coulomb gauge fixed Wilson lines. As the figure shows, the Coulomb gauge data seem to be noisier than the data from Wilson loops. We checked that this is not an artifact of the accuracy at which the Coulomb gauge is fixed. Also the Coulomb gauge results are found to be close to the results from the smeared Wilson loops, but the difference between them is statistically significant.

In the right panel of Fig. 2 we summarize the fitted value of $V_T^{\text{re}}(\vec{r})$ for this set. At this scale, the dependence of the potential on the smearing level is hardly visible. Similarly, the potential from smeared Wilson loops and that from Coulomb gauge fixed Wilson lines are very close, though they differ at the 1σ level.

As we have discussed in Sec. III, we believe that for the study of quarkonia property in medium, the potential from

the smeared Wilson loop is appropriate. It is satisfactory that $V_T^{\text{re}}(\vec{r})$ becomes practically independent of the level of smearing very soon. Anyway, when quoting a result for $V_T^{\text{re}}(\vec{r})$, we include, as a systematic error, some variation with the level of smearing: for example, for the set shown in Fig. 2 we include the spread in results between smearing levels of 100 and 250 as a systematic error. In what follows, our error bars for $V_T^{\text{re}}(\vec{r})$ include this variation for all sets.

Results from lattices at a finite lattice spacing have discretization errors. We can have an idea of the size of the discretization error by comparing the results at different lattice spacings. As Table I shows, we have lattices with three different lattice spacings at $1.2 T_c$, and at $1.5 T_c$ we have results with two different lattice spacings. In Fig. 3 we show the potentials calculated from lattices at different lattice spacings. Within our error bars the results agree very well, indicating that the cutoff effects are very small at these lattice spacings. We will, therefore, take the results on our finest lattice spacings as a valid estimator of the continuum results.

Figure 4 summarizes our results for $V_T^{\text{re}}(\vec{r})$ at different temperatures. We see that the potentials at the two temperatures below T_c agree completely, indicating that the temperature effect is small even at $0.75 T_c$. The potentials have the familiar Cornell form, with a dip at small r and a linearly rising part for $r \gtrsim 0.5$ fm. This behavior changes abruptly on crossing T_c : while the short distance part, $\lesssim 0.2$ fm, remains similar to the form below T_c , beyond $r T_c \sim 0.5 \sim 0.35$ fm the effect of string breaking clearly shows up, and the potential becomes flatter with increasing temperature.

B. Free energy

The study of the free energy cost of introducing a $Q\bar{Q}$ pair in the plasma is almost as old as the study of deconfinement transition in QCD. The free energy of a

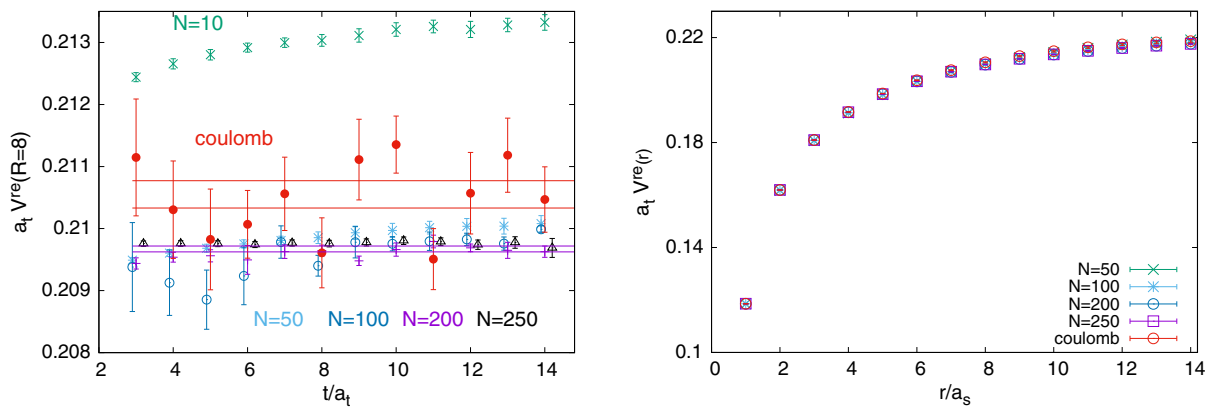


FIG. 2. (Left) The “local measurements” of $V_T^{\text{re}}(\vec{r})$ at $r = 8a_s$, at $T \sim 1.5T_c$, for Set 3. Shown are results from Wilson loops at different levels of smearing, and Coulomb gauge fixed Wilson lines. The horizontal bands show the result for the potential obtained from a single state fit. (Right) Estimates of $V_T^{\text{re}}(\vec{r})$ for the same set, from Wilson loops at different levels of smearing, and for the Coulomb gauge fixed Wilson line.

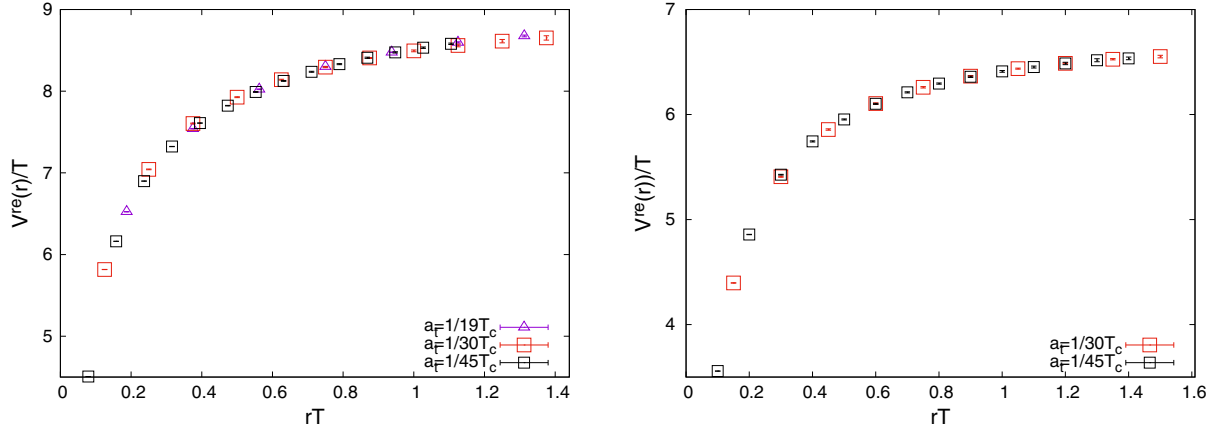


FIG. 3. The potential $V_T^{\text{re}}(\vec{r})$ at (left) $1.2 T_c$, measured on lattices with three different lattice spacings; and (right) at $1.5 T_c$, at two different lattice spacings.

$Q\bar{Q}$ pair was calculated from the correlator of Polyakov loops, $\langle L(\vec{r})L^\dagger(\vec{0}) \rangle$ [35]. Later, the free energy cost of a singlet $Q\bar{Q}$ pair was connected to the cyclic Wilson loop (for sufficiently smeared loops) [36],

$$F(\vec{r}; T) = -T \log W_T(\beta, \vec{r}), \quad (20)$$

or from Coulomb gauge fixed circular Wilson lines [37] (see also [38]). In leading order perturbation theory, the singlet free energy agrees with $V_T^{\text{re}}(\vec{r})$.

The singlet free energy has been studied in great detail, for both gluonic plasma and the theory with quarks [5], and we do not intend to add to the existing results. Here we will, however, examine the issue of whether the perturbative agreement between the free energy and $V_T^{\text{re}}(\vec{r})$ is also valid nonperturbatively.

In Fig. 5 we show the singlet free energy calculated from the smeared circular Wilson loop at different levels of

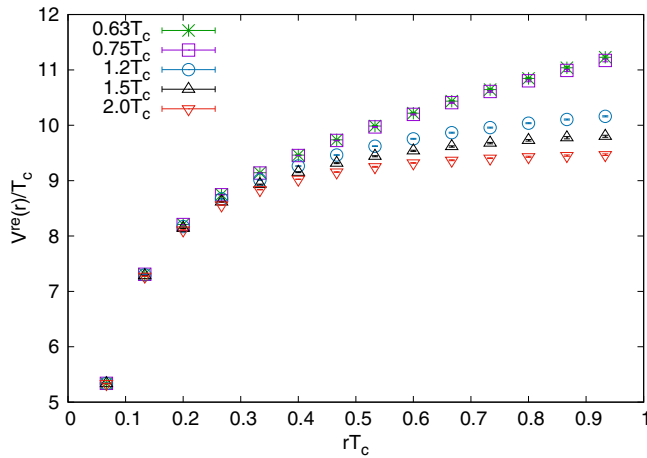


FIG. 4. $V_T^{\text{re}}(\vec{r})$ calculated from smeared Wilson loops. The results are from Set 3, which can be taken as a good estimate of the continuum results.

smearing, and that from the Coulomb gauge fixed operator. The smearing dependence is similar to what was seen for $V_T^{\text{re}}(\vec{r})$: the results are quite insensitive to the smearing level used. The Coulomb gauge operator is close to the Wilson loop results, but not exactly identical.

In Fig. 6 we compare the free energy and $V_T^{\text{re}}(\vec{r})$, extracted from the smeared Wilson loops, at three different temperatures. As discussed before in Sec. IV A, the results are expected to be valid continuum results. At all temperatures, we find that $F(\vec{r}; T)$ and $V_T^{\text{re}}(\vec{r})$ are very close to each other. However, at long distances $V_T^{\text{re}}(\vec{r})$ shows slightly less screened behavior than $F(\vec{r}; T)$.

C. Imaginary part of the potential

As we have discussed in Sec. II, the behavior of the symmetrized correlation function $W_T^p(\tau, \vec{r})$ is dominated by

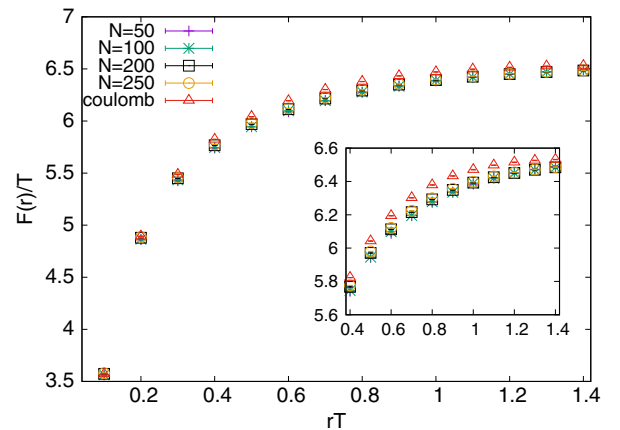


FIG. 5. Free energy calculated from cyclic Wilson loops at different levels of smearing, and from Coulomb gauge fixed circular Wilson lines, at $1.5 T_c$ for Set 2. The inset highlights the long distance part. The Coulomb gauge result is seen to be close to that obtained from a smeared Wilson loop, but with a statistically significant difference.

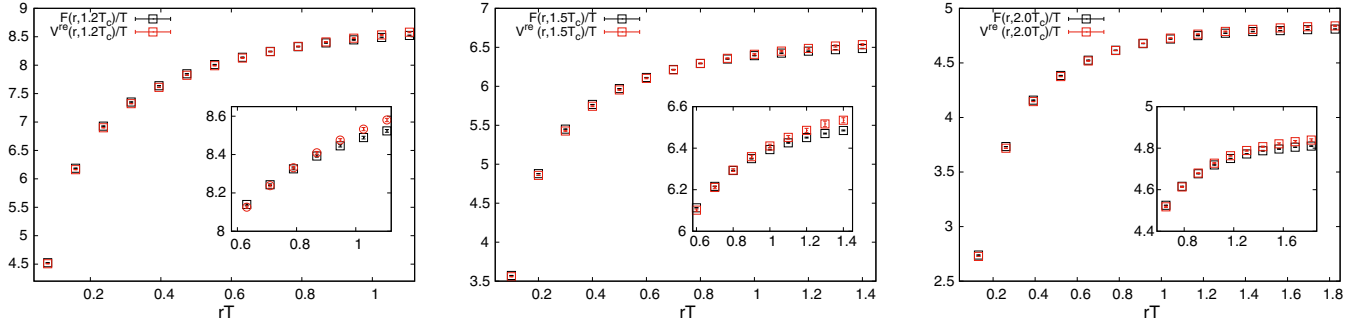


FIG. 6. The free energy, Eq. (20), compared with $V_T^{\text{sc}}(\vec{r})$ at $1.2 T_c$ (left), $1.5 T_c$ (middle), and $2 T_c$ (right). The long distance part is highlighted in the inset.

the most singular behavior in Eq. (17), which is the term that corresponds to $V_T^{\text{im}}(\vec{r})$. Encouraged by this, we expand $\sigma(\omega; T)$ in Eq. (14) in a series

$$\sigma(\omega; T) = (1 + n_B(\omega)) \left(\frac{c_0}{\omega} + c_1 \omega + c_2 \omega^3 + \dots \right), \quad (21)$$

where the form of Eq. (21) is motivated by the structure of $A(\tau, \vec{r})$ [see Eq. (B4) and the discussion at the end of Sec. II]. $\sigma(\omega; T)$ in Eq. (21) has the property that $\sigma(-\omega; T) = e^{-\beta\omega} \sigma(\omega; T)$ and so the integrand in Eq. (14) is an even function of ω ; the even powers of ω are absent in Eq. (21) as they will not contribute to the integral. The imaginary potential $V_T^{\text{im}}(\vec{r})$ is obtained from the coefficient of the $1/\omega$ term: $V_T^{\text{im}}(\vec{r}) = \frac{\pi}{\beta} c_0$. Putting Eq. (21) in Eq. (15), we get the linear series for the ‘‘local mass’’:

$$\begin{aligned} \partial_\tau A(\tau, \vec{r}) &= c_0 \tilde{G}_0(\tau) + \sum_{l=1,2,\dots} c_l \tilde{G}_l(\tau), \\ \tilde{G}_0 &= -\frac{\pi}{\beta} \cot \frac{\pi\tau}{\beta}, \\ \tilde{G}_l &= \frac{(2l)!}{\beta^{2l+1}} \left(\zeta \left(2l+1, 1 - \frac{\tau}{\beta} \right) - \zeta \left(2l+1, \frac{\tau}{\beta} \right) \right), \end{aligned} \quad (22)$$

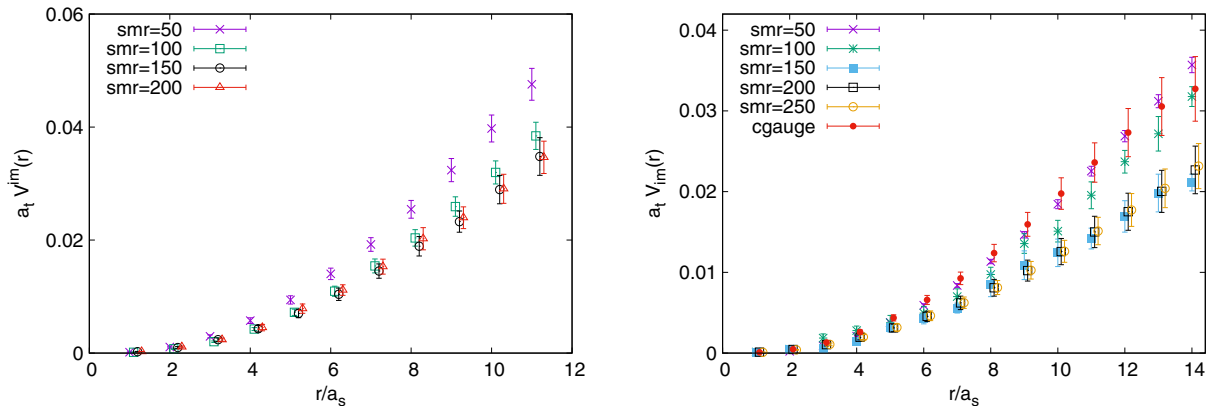


FIG. 7. The imaginary part of the potential, $V_T^{\text{im}}(\vec{r})$, for different smearing levels, (left) at $1.2 T_c$, Set 2, and (right) at $1.5 T_c$, Set 3.

where the generalized ζ functions $\zeta(s, x) = \sum_{n=1}^{\infty} \frac{1}{(x+n)^s}$. Note that this form Eq. (22) is similar to, and could also be motivated by, perturbation theory [8].

The data near $\beta/2$ give a very good fit to just two terms in Eq. (22), and with three terms, almost the entire range of τ could be fit in all our datasets. In Fig. 7 we show the results for $V_T^{\text{im}}(\vec{r})$ obtained with different levels of smearing. The error bar here includes the variation due to the change in number of terms of Eq. (22) in the fit. The dependence on the level of smearing is stronger here, but a plateau can be reached after some levels of smearing. When quoting a result for the imaginary part of the potential in what follows, our error bar encompasses the spread among the different smearing levels in this plateau.

In Fig. 8 we show the imaginary potential at two different temperatures, obtained on lattices with different cutoffs. While our coarsest lattice, Set I, seems to show some lattice spacing dependence, the results from the two finer sets agree very well. We therefore take $V_T^{\text{im}}(\vec{r})$ obtained from our finest lattice as a good approximation to the continuum result.

In Fig. 9 we show our final results for the imaginary potential at three different temperatures. In Sec. V we will use this data as the nonperturbatively evaluated $V_T^{\text{im}}(\vec{r})$ and explore its physics. We have shown here the results above

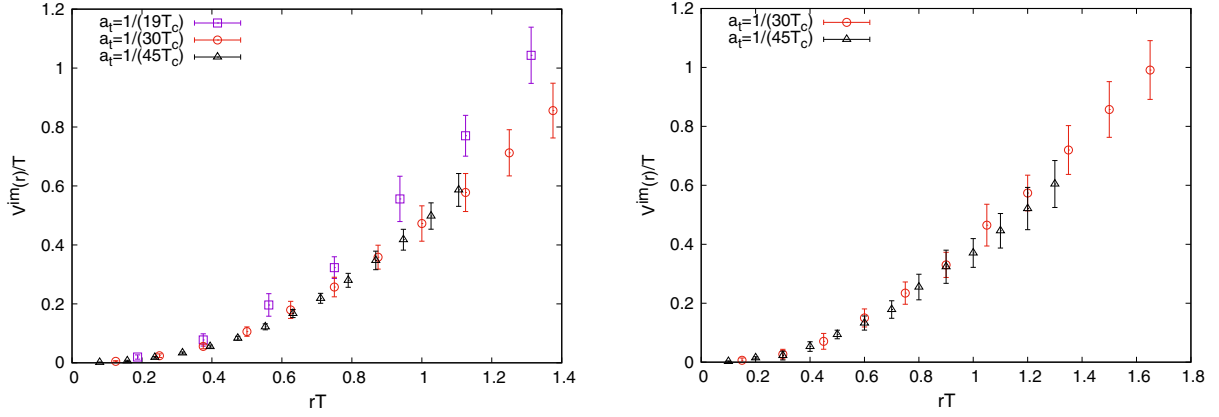


FIG. 8. The imaginary part of the potential, $V_T^{im}(\vec{r})$, at $1.2 T_c$ (left) and at $1.5 T_c$ (right), at different lattice spacings. The results from different lattice spacings vary very little and so we take the results from our finest lattices as a good approximation to the continuum result.

T_c only; we have, however, run the same analysis strategy on the configurations below T_c , and checked that the results are consistent with zero, as expected.

D. Low- ω structure of the spectral function

Combining the results of Sec. IV A and Sec. IV C, we can write the correlation function near the center of the lattice as

$$W_T(\tau, \vec{r}) = e^{-V_T^{re}(\vec{r})(\tau - \frac{\beta}{2}) - \frac{\beta}{\pi} V_T^{im}(\vec{r}) \log \sin(\frac{\pi\tau}{\beta}) - \dots} W_T(\beta/2, \vec{r}), \quad (23)$$

where the higher order terms,

$$\dots = \sum_l c_l \int_{\frac{\beta}{2}}^{\tau} \tilde{G}_l(\tau),$$

do not contribute to the potential. For explaining the Wilson loop data over a substantial range near the center, just c_1 is

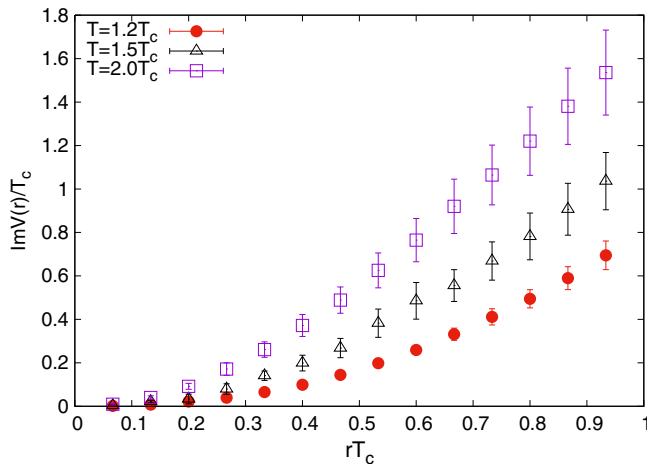


FIG. 9. The imaginary part of the potential, $V_T^{im}(\vec{r})$, extracted from Set 3, at three different temperatures.

enough, while adding c_2 allows us to explain $W_T(\tau, \vec{r})$ over the entire range except a couple of points at the edge.

Further insight into the potential can be obtained if we investigate the structure of the low ω part of $\rho(\omega, \vec{r}; T)$ in Eq. (11). In order to do this, we take the Fourier transform of the structure of $W_T(\tau, \vec{r})$, Eq. (23), continued to real time: $W_T(t = -i\tau, \vec{r})$. This shows a peak structure at low ω , as has been anticipated in various lattice extractions of the potential, e.g., [25,27–29,31]. Interestingly, however, the peak structure is very different from what has often been anticipated. In the literature a Lorentzian or a Gaussian structure has often been assumed for the peak. Instead, we find a structure that is exponentially falling in the low ω side of the peak, $\sim \exp(\omega/T)$, while in the high ω side it falls only as a power law. The illustration of the peak structure is shown for a few representative values of r in Fig. 10. Given this peak structure, we could rephrase our discussion of the potential extraction by simply starting from a structure such as those shown in Fig. 10, and extracting the potential from them. We checked numerically that the Laplace transform of the peak gives a statistically satisfactory description of $W_T(\tau, \vec{r})$ near $\beta/2$. While the direct Bayesian inversions have to grapple with the issue of convergence of the integral in the negative ω side, here we could easily do the integral by putting a lower cutoff: because of the sharp fall, the effect of the cutoff on the value of the integral is negligible. The addition of the correction terms does not have any significant effect on the position or the half-width of the peak, but modifies the falloff with ω away from the position of the peak.

Bayesian statistics based studies of the potential proceed without making strong assumptions about the structure of the peak. In fact, some of the Bayesian analyses use only very mild information about the peak. We would like to add a note of caution here. If we do not make the assumption Eq. (22), which is well-motivated by the physics involved in the imaginary potential and also by perturbation theory, it is possible to describe the Wilson loop data by other

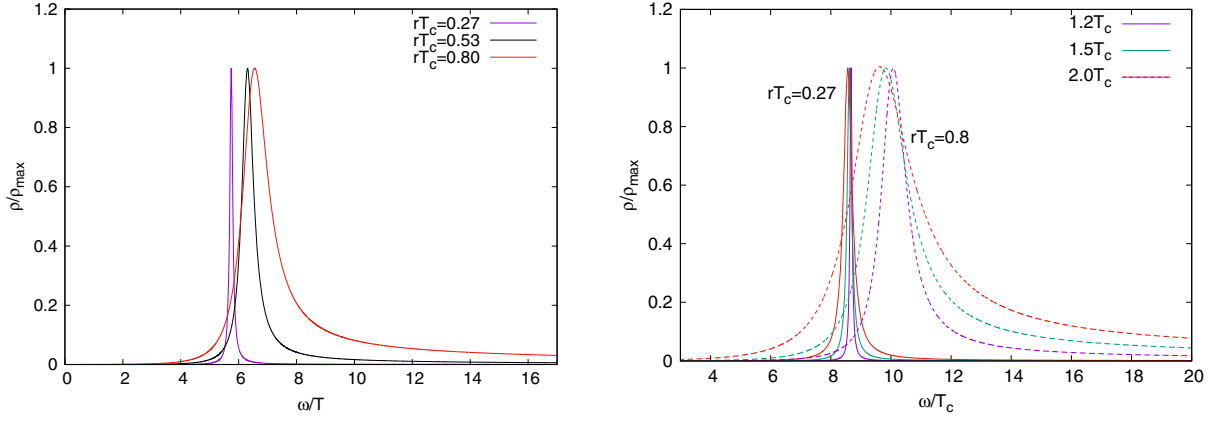


FIG. 10. (Left) The low ω structure of the spectral function obtained from Eq. (23), at $1.5 T_c$. Results for three representative values of r are shown. (Right) The temperature dependence of the low ω peak. results for two values of r are shown.

structures, leading to different $V_T^{\text{im}}(\vec{r})$. In particular, a very good description of the data is provided by the form

$$W_T(\tau, \vec{r}) = e^{-V_T^{\text{re}}(\vec{r})(\tau - \frac{\beta}{2}) - \frac{V_T^{\text{im}}(\vec{r})}{\pi} \int_{\beta/2}^{\tau} \log \frac{\beta - \tau}{\tau} \dots} W_T(\beta/2, \vec{r}). \quad (24)$$

The spectral peak obtained from this form is considerably different from that shown above; see Fig. 11. A Bayesian analysis, in our opinion, ought to include the broad features of the low ω peak discussed in the previous paragraph.

V. DISCUSSION OF POTENTIALS AND QUARKONIA

Let us try to analyze in some detail the potentials obtained in Sec. IV. We start with $V_T^{\text{re}}(\vec{r})$. Figure 4 shows our estimation of $V_T^{\text{re}}(\vec{r})$ at different temperatures. As is expected for a gluonic plasma, the thermal effects are negligible at temperatures of $0.75 T_c$: the potential agrees completely between $0.75 T_c$ and $0.63 T_c$. So the potential at our lowest temperature measured for each set can safely be

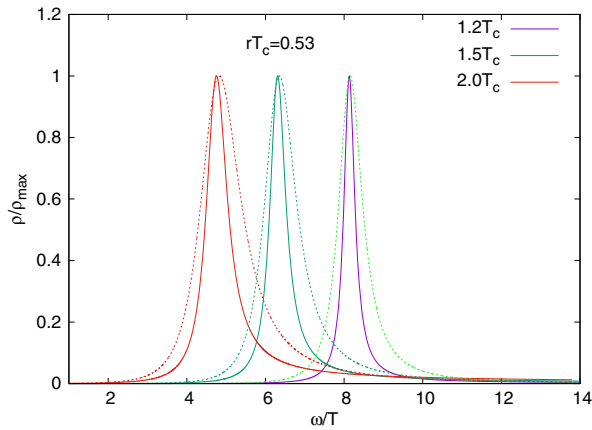


FIG. 11. The low ω structure indicated by Eq. (24) (dotted line) compared with that obtained from Eq. (23), at $R = 8$, at three different temperatures.

taken to approximate the zero-temperature potential. The potential shows the familiar features of the $1/r$ singularity at short distances and the linear rise at large distances, and gives a good fit to the Cornell form.

As we cross T_c , the finite temperature potential is close to that at $T = 0$ at short distances. But clear temperature effects are seen as r increases: in particular, the linear behavior of the $T = 0$ potential gets screened. In perturbation theory one expects, in leading order, a Debye-screened form of $V_T^{\text{re}}(\vec{r})$ which is the same as the free energy [8],

$$V_{\text{pert}}^{\text{re}}(\vec{r}, T) = -\frac{\alpha(T)}{r} e^{-m_D r} - m_D \alpha(T) + C, \quad (25)$$

where $m_D = gT$ in leading order and $\alpha(T)$ is the running coupling at the appropriate temperature scale. In Fig. 12 this form, Eq. (25), is shown at different temperatures, along with the nonperturbatively obtained potential. For drawing the perturbative curve, following [8], we have used a one-loop formula for the coupling [39], $\alpha^{-1}(T) = \frac{33}{8\pi} \log(6.742T/\Lambda_{\overline{\text{MS}}})$, and $T_c/\Lambda_{\overline{\text{MS}}} = 1.10\text{--}1.20$ [40]. The band in the perturbative form in Fig. 12 corresponds to this range in $T_c/\Lambda_{\overline{\text{MS}}}$. Since we are interested in the r dependence of $V_T^{\text{re}}(\vec{r})$, the additive renormalization constant C is fixed by matching to the lattice potential at $rT_c = 0.5$ at $T = 2T_c$.

As Fig. 12 shows, the perturbative form does not explain the potential obtained in Sec. IVA. In particular, the long distance part of the potential is not as flat as the screened Debye form predicts: as if a shadow of the string tension rise survives.

Since the long distance part of the $Q\bar{Q}$ potential in the QCD vacuum has a linear string tension term, a natural next step would be to try a screened form of the string tension term. The string tension term being entirely nonperturbative, there is, however, no single unique/preferred possibility for the screened form of this term. We will consider here two models for screening that have been discussed in the

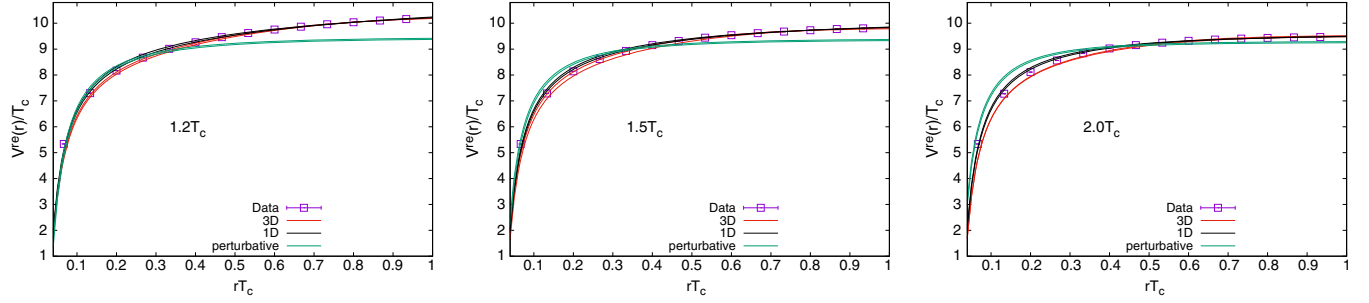


FIG. 12. The finite temperature potential $V_T^{\text{re}}(\vec{r})$ at temperatures $1.2 T_c$ (left), $1.5 T_c$ (middle), and $2 T_c$ (right), shown with various models for the potential: perturbative form [Eq. (25)], Debye-screened string in 1D [Eq. (26)] and in 3D [Eq. (28)].

literature. A linear string tension is obtained in the $(1+1)$ -dimensional Schwinger model. Since string is essentially a one-dimensional (1D) object, one can assume that the physics of screening of the string term will also be similar to that in the Schwinger model. Such a consideration leads to the potential [41]

$$V_{\text{1D}}^{\text{re}}(\vec{r}, T) = -\frac{\alpha}{r} e^{-m_D r} + \frac{\sigma}{m_D} (1 - e^{-m_D r}) + C'. \quad (26)$$

This form of the screened potential can also be obtained by generalizing the timelike gluon propagator to [42]

$$D(p_0 = 0, \vec{p}) \equiv \frac{1}{p^2 + m_D^2} + \frac{2\sigma/\alpha}{(p^2 + m_D^2)^2}. \quad (27)$$

The second term gives a linear string term in the limit $m_D \rightarrow 0$. We treat Eq. (27) here as a purely phenomenological construct to model the screening in a string tension term. In perturbation theory, one expects α to be a function of r and T . In the Cornell potential, however, one usually treats α as a constant. We follow [41] and keep α, σ fixed to their $T = 0$ value, the temperature dependence entering in Eq. (26) only through m_D . The long distance part of the potential $V_T^{\text{re}}(\vec{r})$, Fig. 4, is fitted to Eq. (26) to obtain m_D, C' . $V_{\text{1D}}^{\text{re}}(\vec{r}, T)$ does a good job of explaining the measured potential as shown in Fig. 12. We have tried a few fit ranges covering the large distance side of our measured potential. The band in Fig. 12 shows the variation of the fit parameters on shifting the fit range. The narrowness of the band is evidence for the stability of the fit to the form of Eq. (26). The fitted value of m_D obtained from the fits is shown in Table II; the range corresponds to this change in the fit range.

A different line of argument to a screened potential is to start with a generalized Gauss' law which gives a linear potential [43]. The medium effect then can be incorporated by introducing a medium permittivity [44]. Using an isotropic permittivity motivated by HTL perturbation theory leads to the potential [45]

$$V_{\text{3D}}^{\text{re}}(\vec{r}, T) = -\frac{\alpha}{r} e^{-m_D r} - \frac{\Gamma(1/4)\sigma}{2\pi\mu} \sqrt{x} K_{1/4}\left(\frac{x^2}{2}\right) + C'', \quad (28)$$

where $\mu^2 = m_D \sqrt{\alpha}$, $x = \mu r$, and $K_{1/4}$ is the modified Bessel function of the second kind [46]. At large r , the second term behaves as $\frac{\exp(-x^2/2)}{\sqrt{x}}$. The results of the fit to this form are also shown in Fig. 12 and the value of m_D shown in Table II. The fit to Eq. (26) is found to be slightly more stable than that to Eq. (28), and so we use it for analysis of quarkonia behavior. However, Eq. (28) also approximately captures the r dependence of $V_T^{\text{re}}(\vec{r})$; with our data we cannot statistically rule out either of the one-dimensional and three-dimensional (3D) screening forms.

The imaginary part, $V_T^{\text{im}}(\vec{r})$, turns out to be more difficult to model using the conventional screening forms available in the literature. The perturbative form of the imaginary part, Eq. (9), is shown in Fig. 13 together with our data, for three different temperatures. The parameters used are identical to that for the real part, as detailed below Eq. (25). The data show very different behavior from that of Eq. (9): at short distance, the perturbative result overshoots the data, but it soon saturates, while our non-perturbative data do not show a sign of saturation in the distance scale studied by us. The perturbative result $V_{\text{pert}}^{\text{im}}(\vec{r})$ behaves $\sim r^2 \log r$ at small r , and saturates to

TABLE II. Various parameter sets related to the potential models discussed in Sec. V. The 1D refers to Eq. (26), the 3D to Eq. (28). Also shown are fits to $V_T^{\text{im}}(\vec{r})$ with a quadratic form $V_{\text{fit}}^{\text{im}}(\vec{r}, T) = bT(rT)^2$ and a form $V_{\text{fit}}^{\text{im}}(\vec{r}, T) = a_1 V_{\text{pert}}^{\text{im}}(\vec{r}, T) + a_2 V_{\sigma}^{\text{im}}(\vec{r}, T)$, where $V_{\text{pert}}^{\text{im}}(\vec{r}, T)$ and $V_{\sigma}^{\text{im}}(\vec{r}, T)$ are given in Eq. (9) and Eq. (30), respectively. The errors shown include the variation with a fit range and should be treated as a systematic band rather than a statistical $1 - \sigma$ band.

T/T_c	m_D/T				
	1D	3D	b	a_1	a_2
1.2	1.18(6)	1.37(6)	0.34(1)	-1.23(7)	1.22(4)
1.5	1.34(8)	1.49(6)	0.35(3)	-0.87(2)	1.85(2)
2.0	1.46(8)	1.60(9)	0.29(2)	-0.8(2)	2.85(38)

$\sim \alpha T$ as $r \rightarrow \infty$. The nonperturbative data show a r^2 behavior to a much larger distance: in particular, almost the whole range of r explored by us, $rT_c \lesssim 1$, can be fitted to a quadratic behavior at $1.5 T_c$ and $2 T_c$.

The HTL permittivity that leads to Eq. (9), is complex, so as to produce a complex potential. Use of this permittivity in the generalized Gauss' law leads to [45] Eq. (28) and an imaginary part

$$V_{3D}^{\text{im}}(\vec{r}, T) = V_T^{\text{im}}(\vec{r})_{\text{pert}} + \alpha T \left\{ D_{-1/2}(\sqrt{2}x) \int_0^x dy \text{Re} D_{-1/2}(i\sqrt{2}y) y^2 g\left(\frac{m_D}{\mu} y\right) + \text{Re} D_{-1/2}(i\sqrt{2}x) \int_x^\infty dy D_{-1/2}(\sqrt{2}y) y^2 g\left(\frac{m_D}{\mu} y\right) - D_{-1/2}(0) \int_0^\infty dy D_{-1/2}(\sqrt{2}y) y^2 g\left(\frac{m_D}{\mu} y\right) \right\},$$

$$\text{where } g(x) = \int_0^\infty dz \frac{2z}{z^2 + 1} \frac{\sin zx}{zx}, \quad (29)$$

and

$$D_{-1/2}(z) = \sqrt{\frac{z}{2\pi}} K_{1/4}\left(\frac{z^2}{4}\right)$$

is the parabolic cylinder function. $V_{3D}^{\text{im}}(\vec{r}, T)$ is also shown in Fig. 13, with the legend ‘‘3D.’’ Here the value of m_D obtained from Eq. (28) is used, and the band corresponds to the range in m_D (Table II). This form has a similar behavior $\sim r^2$ at small r to the data. While it is steeper at large r than the perturbative form, it is less steep than our data.

If one uses a complex permittivity analogous to the HTL term in conjunction with the modified propagator of Eq. ([42]), one can get the ‘‘complex potential’’ for 1D screening, i.e., the imaginary part of Eq. (26). The imaginary part reads [42]

$$V_{1D}^{\text{im}}(\vec{r}, T) = V_{\text{pert}}^{\text{im}}(\vec{r}, T) + V_\sigma^{\text{im}}(\vec{r}, T),$$

$$V_\sigma^{\text{im}}(\vec{r}, T) = \frac{4\sigma T}{m_D^2} \int_0^\infty dz \frac{2z}{(z^2 + 1)^3} \left[1 - \frac{\sin(zm_D r)}{zm_D r} \right]. \quad (30)$$

$V_{1D}^{\text{im}}(\vec{r}, T)$ is shown in Fig. 13 with legend ‘‘1D’’; the value of m_D is that obtained from Eq. (26) in Table II. This form seems to have a higher slope than our data at small r and a smaller slope at large r , though at $1.5 T_c$ it is close to our data in the range of r studied by us.

As Fig. 13 reveals, none of the simple forms discussed does a good job of modeling our data for the imaginary potential over the range of r studied by us. At small r , the numerically calculated potential has a smaller slope than either the screened string forms or the forms Eq. (30) and Eq. (29). At large r , on the other hand, it is steeper. Both of these latter forms, in turn, show a much larger imaginary part than the perturbative form at large r , with Eq. (30) comparable to our data at larger values of r . In the range $rT_c \lesssim 1$ studied here, our data for $V_T^{\text{im}}(\vec{r})$ grows $\sim r^2$. On physical principles we expect it to saturate at large r . Motivated by Eq. (30), we tried to model the imaginary part of the potential by fitting the data to an arbitrary combination $a_1 V_{\text{pert}}^{\text{im}}(\vec{r}, T) + a_2 V_\sigma^{\text{im}}(\vec{r}, T)$. The results of the fit are shown in Table II, which also shows the results of the fit to a purely quadratic form $bT(rT)^2$. We emphasize that our forms for $V_{\text{fit}}^{\text{im}}(\vec{r}, T)$ represent purely phenomenological fits of the data; one can take them to correspond to two limiting asymptotic behaviors given the data.

To get an idea of the effect of the imaginary part at various quark masses, let us calculate the spectral function of the $\bar{Q}\gamma_\mu Q$ current at various values of M_Q using Eqs. (4) and (6), with

$$V_{Q\bar{Q}}(\vec{r}, T) = V_{1D}^{\text{re}}(\vec{r}, T) - iV_{\text{fit}}^{\text{im}}(\vec{r}, T), \quad (31)$$

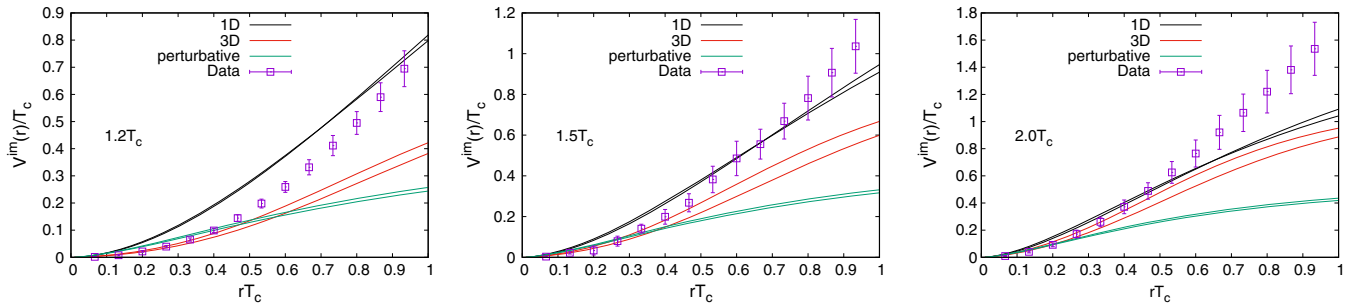


FIG. 13. The imaginary part of the finite temperature potential, $V_T^{\text{im}}(\vec{r})$, at temperatures $1.2 T_c$ (left), $1.5 T_c$ (middle), and $2 T_c$ (right), shown with various models for the potential: perturbative form [Eq. (9)], Debye-screened string in 1D [Eq. (30)] and in 3D [Eq. (29)].

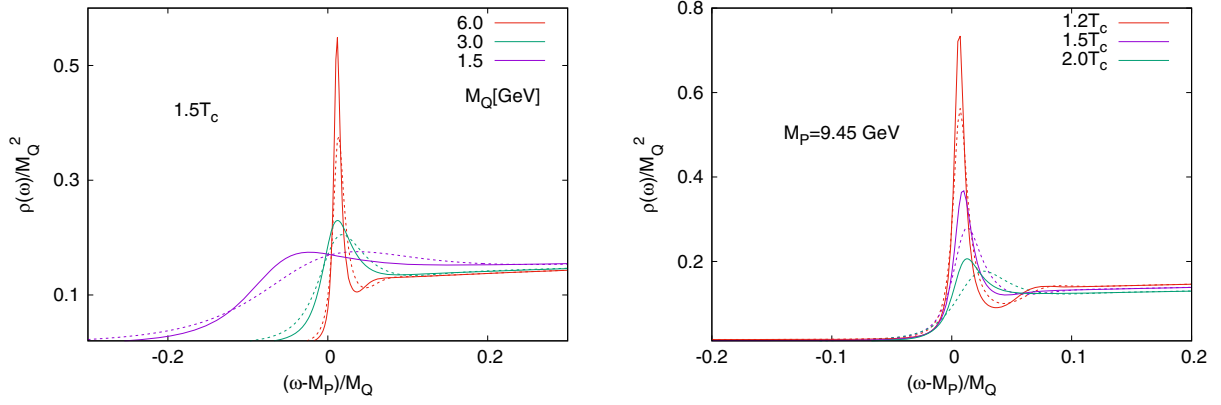


FIG. 14. (Left) the peak of the spectral function $\rho(\omega, \vec{r} \rightarrow 0)$ for a $\bar{Q}\gamma_\mu Q$ current probe in an equilibrated plasma at a temperature of $1.5 T_c$, for different values of the quark mass. The dashed line corresponds to the quadratic form and the full line to the two-parameter form of $V_T^{\text{im}}(\vec{r})$. (Right) The spectral function at different temperatures for a quark mass close to the bottom, $M(1S) = 9.45$ GeV. In the x axis, the zero is at $\omega = M_P$, the 1S state mass obtained using the Cornell potential.

where $V_{\text{ID}}^{\text{re}}(\vec{r}, T)$ is given in Eq. (26) and for $V_{\text{fit}}^{\text{im}}(\vec{r}, T)$ we use the two fit forms with the fit parameters given in Table II, treating the results obtained with the two forms of $V_T^{\text{im}}(\vec{r})$ as a systematic band. As mentioned in the Introduction, this corresponds to an idealized situation of an external heavy quark current probe in an equilibrated plasma [11,22]. A dynamical study of quarkonia in plasma requires a more elaborate formalism [12,23,24]. However, the spectral function obtained here can be compared to lattice studies of quarkonia spectral functions for charm [15,16] and bottom [17,18]. In the left panel of Fig. 14 we have shown the spectral function obtained using Eq. (31) at $1.5 T_c$, with the quark mass varying from 1.5 GeV to 6 GeV. At $T = 0$, using the unscreened Cornell potential we get a series of sharp peaks. We denote the mass of the 1S state as M_P and normalize the x axis with respect to it in Fig. 14. At $1.5 T_c$, even for a quark mass of 6 GeV we only find one peak. Of course, $1.5 T_c$ here corresponds to a temperature of about 420 MeV. Expectedly, the peak is the sharpest for the heaviest quark, gradually broadening till, for quark masses close to the charm, only a very broad peak structure can be seen. The spectral function for $M_Q = 1.5$ GeV is also qualitatively different from the others, and it is very different from the spectral function obtained directly from $\bar{c}\gamma_\mu c$ correlators in [15], but in qualitative agreement with a later study [16]. Similar results have been seen in [20]. In the right panel of Fig. 14 we have shown the peak in the spectral function of the $\bar{b}\gamma_\mu b$ current. Quark mass M_Q was tuned to get the 1S state mass (in vacuum) ~ 9.45 GeV. A sharp peak is seen at $1.2 T_c$, which gradually broadens as the temperature increases. But a peak structure survives all the way to $2 T_c$. Note that $2 T_c$ here corresponds to about 560 MeV, setting the scale using the string tension. Also at low temperatures the peak is quite narrow, in comparison to what was found from nonrelativistic bottomonia correlators in [17].

VI. SUMMARY

For the study of quarkonia in quark-gluon plasma, an effective “in-medium potential” is an important ingredient. Theoretically, a suitable potential can be defined [8,9] by examining the time dependence of the Minkowski-time Wilson loop, Eq. (8). This potential is complex, with the real part of the potential describing the Debye-screened binding of the $Q\bar{Q}$ pair in medium and the imaginary part related to Landau damping. A nonperturbative extraction of this potential [25] involves extracting the low-frequency structure of the spectral function from the Euclidean-time Wilson loop, Eq. (11). This is in general a very difficult problem. The existing studies in the literature have progressed through either by using Bayesian analysis, with their associated, and sometimes hard-to-estimate, systematic errors, or by making an *ad hoc* assumption about the low-frequency structure.

In this work we have introduced a new method of nonperturbative evaluation of the potential. We find that a reorganization of the Euclidean Wilson loop data, motivated by the underlying structure of the finite temperature correlation function (see Appendix B), leads to an enormous simplification in the extraction of the peak structure from the Wilson loop. The main ingredients of our method are outlined in Sec. II, and the details are given in Sec. IV. We have calculated the potential in a gluonic plasma for temperatures $\leq 2T_c$ from smeared Wilson loops, calculated using anisotropic lattice discretization of the gluonic theory. Our results for the potential are summarized in Fig. 4 and Fig. 9. The real part of the potential, which shows the Cornell form below T_c with no noticeable temperature dependence up to $0.75 T_c$, shows Debye screening on crossing T_c , with the screening mass increasing with temperature. The form of the potential is different from the perturbative form at least up to $2 T_c$, as illustrated in Fig. 12. The imaginary part of the potential is zero below

T_c . Above T_c it rises rapidly, with a spatial dependence $\sim r^2$ till distances $r \lesssim 1/T_c$. Its behavior is sharply different from the perturbative result, as illustrated in Fig. 13.

In the course of our study, we have also investigated issues such as the dependence of the finite-temperature potential on the definition of the operator, which, we feel, have not been properly discussed in the literature. We have examined how the potential depends on the smearing and compared the potential obtained from smeared Wilson loops with those from Coulomb gauge fixed Wilson line correlators. We have also examined the relation between the real part of the potential and the free energy of a static $Q\bar{Q}$ pair in the plasma; see Fig. 6. In Sec. IV D we have discussed the structure of the low energy peak of the spectral function. It is quite different from the Lorentzian structure that has often been assumed in direct extractions of potential from the Euclidean Wilson loop using Eq. (11). We have also illustrated, with an example, the difficulty of extracting the low energy peak from the Euclidean Wilson loop without putting in additional physics input.

Our data for the extracted potential can be found in Sec. IV, in particular in Fig. 4 and Fig. 9. Moreover, for various purposes it is convenient to have a parametrization of the potential. In Sec. V we have explored various standard forms of a screened potential. As Fig. 12 shows, for the real part, the form of 1D screening of the string potential seems to give a reasonable description of the data, with parameters given in Table II. For the imaginary part it is more difficult to find a quantitative agreement with a standard screened form. The potential rises $\sim r^2$ till intermediate distances $rT_c \sim 1$. While the potential is expected to saturate as $r \rightarrow \infty$, it is difficult to make any statement about that behavior from our data at $rT_c \lesssim 1$. A purely phenomenological generalization of Eq. (30), using an arbitrary linear combination of $V_T^{\text{im}}(\vec{r})_{\text{pert}}$ and $V_T^{\text{im}}(\vec{r})_{\sigma}$, seems to give a good description of the data in the range of r explored by us, with coefficients given in Table II. Since we expect the long distance behavior of $V_T^{\text{im}}(\vec{r})$ to be somewhere between this and the r^2 behavior, for a study of the spectral peaks of $\bar{Q}\gamma_\mu Q$ current in the plasma we use both of the forms for $V_T^{\text{im}}(\vec{r})$. The difference in the spectral structure obtained with these two forms is considered as a qualitative systematic band.

The spectral function peaks for a vector current probe in the equilibrated plasma are shown in Fig. 14. In the left panel, the variation of the spectral function with the heavy quark mass, M_Q , is shown. Below T_c the spectral function has a number of narrow peaks corresponding to the nS states; but above T_c only a single peak near $2M_Q$ survived even for $M_Q = 6$ GeV. For $M_Q = 1.5$ GeV, close to the mass of charm, there is no significant peak structure at this temperature. Of course, the nonrelativistic formalism may not be valid for charmonia at these temperatures. For $M_Q = 3$ GeV, a clear peak structure is seen at $1.5 T_c$,

with very little shift in the peak position. In the right panel of Fig. 14 the spectral function peak for $\bar{b}\gamma_\mu b$ current is shown. While the peak structure weakens with temperature, a clear peak survives till $2 T_c$, with very little shift in peak position, and a reasonably narrow peak, at least till $1.5 T_c$.

While potential by itself does not provide a complete description of medium interaction of quarkonia, it is an important part of a complete description. It provides essential nonperturbative ingredients of an open quantum system analysis of in-medium quarkonia [11–13,22–24]. It can also provide a useful benchmark for direct extraction of spectral functions from Matsubara correlators calculated on lattice. Our results are for the quenched theory, and one needs to be careful when applying them for quarkonia phenomenology. However, the method we have outlined for the extraction of the potential, Sec. II, is quite simple and stable, and we expect one should be able to use it to extract the reliable potential also from dynamical lattices.

ACKNOWLEDGMENTS

We acknowledge support of the Department of Atomic Energy, Government of India, under Project No. 12-R&D-TFR-5.02-0200. This work was carried out under the umbrella of ILGTI. The computations reported here were performed on the clusters of the Department of Theoretical Physics, TIFR. We thank Ajay Salve and Kapil Ghadiali for technical support. D.B. thanks Rajiv Gavai, Alexander Rothkopf, and Peter Petreczky for discussions.

APPENDIX A: LATTICE PARAMETERS

We use the anisotropic Wilson gauge action for our discretization of the gluonic theory. The discretized Euclidean action is

$$S_G = \frac{\beta_s}{N} \sum_{ij} \text{Re tr}(1 - P_{ij}(x)) + \frac{\beta_\tau}{N} \sum_i \text{Re tr}(1 - P_{4i}(x)), \quad (\text{A1})$$

where $i, j = 1, 2, 3$ and $P_{\mu\nu}$ are the plaquette variables in the μ, ν direction. Since we are interested in fine grating in the time direction, we use $\beta_\tau \gg \beta_s$.

Klassen has provided a convenient way of nonperturbatively finding couplings suitable for an anisotropy, $\xi = a_s/a_\tau$, from the comparison of spatial and spacetime Wilson loops [32]: find $\xi_0 = \sqrt{\beta_\tau/\beta_s}$ such that

$$\frac{R(x, y)}{R(x, t = \xi y)} = 1 \quad \text{where } R(i, j) = \frac{W(i, j)}{W(i+1, j)}. \quad (\text{A2})$$

An interpolating formula for estimating β_s and β_τ for a given ξ is also given [32]. We use this formula to get the suitable couplings for our purpose and then checked the anisotropy by comparing the potentials as mentioned

above. We use this formula to get a set of prior guesses for lattices with $\xi = 3$, and then did some simulations to tune the anisotropy. The final parameter set for our runs is shown in Table I.

For each of the lattices in Table I we have used about $\mathcal{O}(10^4)$ configurations. For each set, the configurations were generated from 90 independent (different random number seeds) runs. For the runs below T_c , a multilevel algorithm was used. About 2000 measurements were collected (90 independent runs with 20–25 measurements each), with each measurement being a sublattice average of 200–400 updates, and after each measurement 100 decorrelating sweeps were made. Each sweep consisted of one heat bath and three overrelaxation steps (this was kept fixed across all runs). The above T_c multilevel was less cost effective and was used mostly for the runs with large N_τ . The multilevel steps were similar to what is described above, but a larger number of measurements ~ 4500 – 9000 were used. In the runs above T_c where multilevel was not used, 9000–27000 configurations were used, two configurations being separated by 100 sweeps.

APPENDIX B: PERTURBATIVE EXPRESSIONS

In Sec. II we have outlined our method to extract the thermal potential, Eq. (6). At $T = 0$ the definition of $V(\vec{r})$ through Eq. (8) is well understood diagrammatically: the ladder of time-ordered gluon propagators D_{00} (including the crossed diagrams) lead to an exponentiation of the Fourier transform of $D_{00}(0, \vec{k})$, which defines the potential [47].

At finite temperature, the structure of the Wilson loop is more complicated. It was stressed in [9], however (and demonstrated for QED), that in order for a potential to exist via Eq. (8) the ladder of the time-ordered gluon propagators need to be resummed. Then $W_M(t, \vec{r})$ will have the structure

$$W_M(t, \vec{r}_1, \vec{r}_2) \sim e^{-i \int_0^t dt_1 \int_0^t dt_2 D_T^{00}(t_1 - t_2, \vec{r}_1 - \vec{r}_2)}. \quad (\text{B1})$$

Here we have only shown the potential part that depends on $\vec{r}_1 - \vec{r}_2$, omitting self-energy corrections and nonpotential contributions.

The Euclidean Wilson loop can, similarly, be written as [9]

$$W_T(\tau, \vec{r}) \sim e^{-\int_0^\tau d\tau_1 \int_0^\tau d\tau_2 \Delta(\tau_1 - \tau_2, \vec{r})}, \quad (\text{B2})$$

where the finite-temperature imaginary-time propagator has the structure [9]

$$\Delta(\tau, \vec{r}) = \int \frac{d\omega}{2\pi} e^{-\omega\tau} \rho_D(\omega, \vec{r}) [\theta(\tau) + n_B(\omega)]. \quad (\text{B3})$$

Here we have used a mixed representation in the right-hand side: $\rho_D(\omega, \vec{r})$ is the spatial Fourier transform of the usual spectral function.

Putting Eq. (B3) in Eq. (B2) gives, using $n_B(\omega) = e^{-\beta\omega}(1 + n_B(\omega))$,

$$\begin{aligned} \log W_T(\tau, \vec{r}) \sim & \int \frac{d\omega}{2\pi} \tau \frac{\rho_D(\omega, \vec{r})}{\omega} \\ & + \int \frac{d\omega}{2\pi} (1 + n_B(\omega)) (e^{-\omega\tau} + e^{-\omega(\beta-\tau)}) \\ & \times \frac{\rho_D(\omega, \vec{r})}{\omega^2}, \end{aligned} \quad (\text{B4})$$

omitting τ independent terms. The first and second terms in the right-hand side of Eq. (B4) correspond to $B(\tau, \vec{r})$ and $A(\tau, \vec{r})$ in Sec. II.

For QCD, the expression for the Wilson loop has been calculated in [8] to leading order in HTL perturbation theory. For convenience, we reproduce here the results of [8], written in the notation of Sec. II,

$$\begin{aligned} A(\tau, \vec{r}) = & 2g^2 c_f \int \mathbf{d}\mathbf{q} \sin^2 \frac{q_3 r}{2} (1 + n_B(\omega)) (e^{-\omega\tau} + e^{-(\beta-\tau)\omega}) \\ & \times \left\{ \left(\frac{1}{\vec{q}^2} - \frac{1}{\omega^2} \right) \rho_E(\omega, \vec{q}) + \left(\frac{1}{\vec{q}_3^2} - \frac{1}{\vec{q}^2} \right) \rho_T(\omega, \vec{q}) \right\} \\ & + \tau \text{ indep. terms}, \\ B(\tau, \vec{r}) = & 2g^2 c_f \int \mathbf{d}\mathbf{q} \sin^2 \frac{q_3 r \beta / 2 - \tau}{2} \frac{\rho_E(\omega, \vec{q})}{\omega}. \end{aligned} \quad (\text{B5})$$

Here $\mathbf{d}\mathbf{q} = \frac{d^3 q}{(2\pi)^3} \frac{d\omega}{\pi}$, $c_f = \frac{4}{3}$ is the color factor, and $\rho_T(\omega, \vec{q})$, $\rho_E(\omega, \vec{q})$ are the spectral functions corresponding to the transverse and the longitudinal parts of the gluon propagator.

We are interested in the energy regime $|\omega| \ll |\vec{q}|$. In this regime, the spectral functions $\rho_E(\omega, \vec{q})$, $\rho_T(\omega, \vec{q})$ become, to leading order in HTL perturbation theory,

$$\begin{aligned} \rho_E(\omega, \vec{q}) = & -\pi m_D^2 \frac{\omega}{2|\vec{q}|(\omega^2 + m_D^2)^2}, \\ \rho_T(\omega, \vec{q}) = & \pi m_D^2 \frac{\omega}{4|\vec{q}|^5}. \end{aligned} \quad (\text{B6})$$

- [1] G. S. Bali, *Phys. Rep.* **343**, 1 (2001).
- [2] N. Brambilla, A. Pineda, J. Soto, and A. Vairo, *Rev. Mod. Phys.* **77**, 1423 (2005).
- [3] T. Matsui and H. Satz, *Phys. Lett. B* **178**, 416 (1986).
- [4] F. Karsch, M. T. Mehr, and H. Satz, *Z. Phys. C* **37**, 617 (1988); S. Digal, P. Petreczky, and H. Satz, *Phys. Rev. D* **64**, 094015 (2001); W. M. Alberico, A. Beraudo, A. De Pace, and A. Molinari, *Phys. Rev. D* **72**, 114011 (2005).
- [5] O. Kaczmarek, F. Karsch, P. Petreczky, and F. Zantow, *Phys. Lett. B* **543**, 41 (2002); O. Kaczmarek and F. Zantow, *Phys. Rev. D* **71**, 114510 (2005); *Eur. Phys. J. C* **43**, 59 (2005).
- [6] O. Kaczmarek, F. Karsch, P. Petreczky, and F. Zantow, *Nucl. Phys. B, Proc. Suppl.* **129**, 560 (2004).
- [7] C.-Y. Wong, *Phys. Rev. C* **72**, 034906 (2005).
- [8] M. Laine, O. Philipsen, P. Romatschke, and M. Tassler, *J. High Energy Phys.* **03** (2007) 054.
- [9] A. Beraudo, J.-P. Blaizot, and C. Ratti, *Nucl. Phys.* **A806**, 312 (2008).
- [10] Y. Burnier, M. Laine, and M. Vepsäläinen, *J. High Energy Phys.* **01** (2008) 043.
- [11] Y. Akamatsu and A. Rothkopf, *Phys. Rev. D* **85**, 105011 (2012).
- [12] S. Kajimoto, Y. Akamatsu, M. Asakawa, and A. Rothkopf, *Phys. Rev. D* **97**, 014003 (2018).
- [13] Y. Akamatsu, *Phys. Rev. D* **91**, 056002 (2015).
- [14] N. Brambilla, J. Ghiglieri, A. Vairo, and P. Petreczky, *Phys. Rev. D* **78**, 014017 (2008).
- [15] M. Asakawa and T. Hatsuda, *Phys. Rev. Lett.* **92**, 012001 (2004); S. Datta, F. Karsch, P. Petreczky, and I. Wetzorke, *Phys. Rev. D* **69**, 094507 (2004); T. Umeda, K. Nomura, and H. Matsufuru, *Eur. Phys. J. C* **39**, 9 (2005).
- [16] H. T. Ding, A. Francis, O. Kaczmarek, F. Karsch, H. Satz, and W. Soeldner, *Phys. Rev. D* **86**, 014509 (2012).
- [17] G. Aarts, C. Allton, S. Kim, M. P. Lombardo, M. B. Oktay, S. M. Ryan, D. K. Sinclair, and J. I. Skullerud, *J. High Energy Phys.* **11** (2011) 103.
- [18] S. Kim, P. Petreczky, and A. Rothkopf, *J. High Energy Phys.* **11** (2018) 088.
- [19] A. Mocsy, P. Petreczky, and M. Strickland, *Int. J. Mod. Phys. A* **28**, 1340012 (2013); S. Datta, *Pramana* **84**, 881 (2015).
- [20] A. Mocsy and P. Petreczky, *Phys. Rev. D* **77**, 014501 (2008).
- [21] X. Du, M. He, and R. Rapp, *Phys. Rev. C* **96**, 054901 (2017); B. Krouppa, A. Rothkopf, and M. Strickland, *Phys. Rev. D* **97**, 016017 (2018); X. Du, S. Y. F. Liu, and R. Rapp, *Phys. Lett. B* **796**, 20 (2019).
- [22] J. P. Blaizot, D. De Boni, P. Faccioli, and G. Garberoglio, *Nucl. Phys.* **A946**, 49 (2016).
- [23] N. Brambilla, M. A. Escobedo, J. soto, and A. Vairo, *Phys. Rev. D* **97**, 074009 (2018).
- [24] T. Miura, Y. Akamatsu, M. Asakawa, and A. Rothkopf, *arxiv:1908.06293*.
- [25] A. Rothkopf, T. Hatsuda, and S. Sasaki, *Phys. Rev. Lett.* **108**, 162001 (2012).
- [26] M. Lüscher and P. Weisz, *J. High Energy Phys.* **09** (2001) 010.
- [27] Y. Burnier, O. Kaczmarek, and A. Rothkopf, *Phys. Rev. Lett.* **114**, 082001 (2015).
- [28] Y. Burnier and A. Rothkopf, *Phys. Rev. D* **86**, 051503(R) (2012).
- [29] Y. Burnier and A. Rothkopf, *Phys. Rev. D* **95**, 054511 (2017).
- [30] P. Petreczky and J. weber, *Nucl. Phys.* **A967**, 592 (2017).
- [31] P. Petreczky, A. Rothkopf, and J. weber, *Nucl. Phys.* **A982**, 735 (2019).
- [32] T. R. Klassen, *Nucl. Phys.* **B533**, 557 (1998).
- [33] M. Albanese *et al.*, *Phys. Lett. B* **192**, 163 (1987).
- [34] J. C. Vink and U.-J. Wiese, *Phys. Lett. B* **289**, 122 (1992); O. Philipsen, *Phys. Lett. B* **535**, 138 (2002).
- [35] L. D. McLerran and B. Svetitsky, *Phys. Rev. D* **24**, 450 (1981).
- [36] A. Bazavov, N. Brambilla, P. Petreczky, and A. vairo, *Phys. Rev. D* **98**, 054511 (2018).
- [37] S. Nadkarni, *Phys. Rev. D* **34**, 3904 (1986).
- [38] O. Jahn and O. Philipsen, *Phys. Rev. D* **70**, 074504 (2004).
- [39] K. Kajantie, M. Laine, K. Rummukainen, and M. Shaposhnikov, *Nucl. Phys.* **B458**, 90 (1996).
- [40] S. Datta and S. Gupta, *Phys. Rev. D* **80**, 114504 (2009).
- [41] F. Karsch, M. T. Mehr, and H. Satz, *Z. Phys. C* **37**, 617 (1988).
- [42] Y. Guo, L. Dong, J. Pan, and M. R. Moldes, *Phys. Rev. D* **100**, 036011 (2019).
- [43] V. V. Dixit, *Mod. Phys. Lett. A* **05**, 227 (1990).
- [44] L. Thakur, U. Kakade, and B. K. Patra, *Phys. Rev. D* **89**, 094020 (2014).
- [45] Y. Burnier and A. Rothkopf, *Phys. Lett. B* **753**, 232 (2016).
- [46] A somewhat similar form, with however $K_{1/4}(x^2)$, is obtained by introducing the medium effect through linearized Boltzmann distribution instead [43].
- [47] W. Fischler, *Nucl. Phys.* **B129**, 157 (1977).